SUPERCONDUCTIVITY

Dynamical charge density fluctuations pervading the phase diagram of a Cu-based high-T_c superconductor

R. Arpaia[1,2]*, S. Caprara[3,4], R. Fumagalli[1], G. De Vecchi[1], Y. Y. Peng[1]†, E. Andersson[2], D. Betto[5], G. M. De Luca[6,7], N. B. Brookes[5], F. Lombardi[2], M. Salluzzo[7], L. Braicovich[1,5], C. Di Castro[3,4], M. Grilli[3,4], G. Ghiringhelli[1,8]*

Charge density modulations have been observed in all families of high–critical temperature (T_c) superconducting cuprates. Although they are consistently found in the underdoped region of the phase diagram and at relatively low temperatures, it is still unclear to what extent they influence the unusual properties of these systems. Using resonant x-ray scattering, we carefully determined the temperature dependence of charge density modulations in YBa$_2$Cu$_3$O$_{7−δ}$ and Nd$_{1+x}$Ba$_{2−x}$Cu$_3$O$_{7−δ}$ for several doping levels. We isolated short-range dynamical charge density fluctuations in addition to the previously known quasi-critical charge density waves. They persist up to well above the pseudogap temperature $T*$, are characterized by energies of a few milli–electron volts, and pervade a large area of the phase diagram.

Cuprate high-temperature superconductors (HTSs) deviate from the Landau Fermi liquid paradigm as a result of the quasi–two-dimensionality of their layered structure and the large electron-electron repulsion. The doping (p)–temperature (T) phase diagram encompasses, at low T, the antiferromagnetic and the superconducting orders and, at higher T, the pseudogap region, which is characterized by a reduction of the quasi-particle density of states in some sections of the Fermi surface below the crossover temperature $T*$. In the pseudogap state and up to optimal doping p ~ 0.17, short- to medium-range incommensurate charge density wave (CDW) order emerges and competes weakly with superconductivity. Theoretical proposals of CDW (1–3) and of low-energy charge fluctuations (4) were first put forward not long after the discovery of HTS; experimental evidence from surface and bulk sensitive techniques came initially in selected materials (5–8) and later in all cuprate families (9–14). Moreover, long-range tridimensional CDW (3D CDW) order has been observed inside the superconducting dome (for p ~ 0.08 to 0.17) in special circumstances, such as in high magnetic fields that weaken superconductivity or in epitaxially grown samples (15–17). Finally, the recent observation of charge density modulations in overdoped (Bi,Pb)$_{2.12}$Sr$_{1.88}$CuO$_{6+δ}$ outside the pseudogap regime (18) hints at a wider than expected occurrence of this phenomenon.

The relevance of charge density modulations for the unconventional normal state and the superconducting properties of HTS is currently being debated. In some theoretical models, long- and short-range CDW orders are seen as epiphenomena on top of a fundamentally peculiar metallic state, where the endpoint at T = 0 of the pseudogap boundary line ($p*$ ~ 0.19 to 0.21) marks the physical onset of a non–Fermi liquid metallic phase (19–24). In alternative scenarios, charge density modulations are instead pivotal to the anomalous properties of cuprates (1, 25–27). In such scenarios, CDW orders are expected to be critical [i.e., associated with the divergence of a correlation length at a quantum critical point (QCP)] and to permeate, through charge density fluctuations (CDFs), a much broader area of the phase diagram. In this context, short-range correlations extending up to room temperature have recently been observed in the electron-doped cuprate Nd$_{2−x}$Ce$_x$CuO$_4$ (13). To establish to what extent static and fluctuating charge density modulations contribute to the phase diagram, we have measured them in YBa$_2$Cu$_3$O$_{7−δ}$ and Nd$_{1+x}$Ba$_{2−x}$Cu$_3$O$_{7−δ}$ as a function of doping and temperature. We have discovered that CDFs are present over a broad region of the phase diagram, which strengthens the importance of charge density modulations in determining the normal-state properties of cuprates; additionally, our findings are consistent with the previously known short- to medium-range CDW orders being precursors of the long-range charge modulation detected in the presence of high magnetic fields, pointing toward CDW orders as a quasi-critical phenomenon.

We measured resonant inelastic x-ray scattering (RIXS) on five YBa$_2$Cu$_3$O$_{7−δ}$ (YBCO) and Nd$_{1+x}$Ba$_{2−x}$Cu$_3$O$_{7−δ}$ (NBCO) thin films spanning a broad range of oxygen doping, going from the antiferromagnetic (AF) region, where $T*$ is not even defined, passing through the underdoped (UD) and the optimally doped (OP) regime, up to the slightly overdoped region (i.e., beyond the pseudogap line) (fig. S1) (28–30). Measurements were performed at the Cu L_3 edge (~930 eV), over broad in-plane wave vector ranges ($q_{||}$ = 0.2 to 0.4 reciprocal lattice units, r.l.u.) and temperature ranges (T = 20 to 270 K). Figure 1C shows the quasi-elastic (near-zero energy loss) component of the RIXS spectra as a function of $q_{||}$ = (H, 0) taken on sample UD60 (NBCO, $p ≈ 0.11$) at different temperatures. A clear peak is present in the whole temperature range under investigation. The intensity of the peak decreases as the temperature increases, with little temperature dependence above 200 K. A quasi-elastic peak, robust versus temperature, is also present in samples UD81 (YBCO, $p ≈ 0.14$; Fig. 1B) and OP90 (NBCO, $p ≈ 0.17$; Fig. 1A). In contrast, the antiferromagnetic sample (NBCO AF) shows no peaks above the linear background (Fig. 1D). These data highlight the existence of a genuine quasi–T-independent scattering signal representative of short-range charge modulations; although this peak was present in previously published x-ray scattering data on YBCO, Bi$_2$Sr$_{2−x}$La$_x$CuO$_{6+δ}$, La$_{2−x}$Sr$_x$CuO$_4$, and other cuprates, it had been considered to be part of the "high-temperature" background and subtracted out; consequently, it had not been thoroughly discussed (10, 12, 31–33). Note that no peak is present in the (H, H) direction, where a featureless linear shape is observed that can be used as a linear background in the fitting of the scans along (H, 0) (Fig. 2, A to C). The scattering peak intensity is approximately linear versus $1/T$ (Fig. 1C, inset): The extrapolation to very high temperature ($1/T$ = 0) provides an estimate of the intrinsic background of the signal, stemming mainly from the scattering from low-energy phonons and surface imperfections (fig. S3) (28).

We decomposed the (H, 0) scans by least-squares fitting to extract the peak intensity, width, and position. Figure 2 shows the results for sample UD60. At high temperatures, the quasi-elastic intensity can be fitted by assuming a single, broad Lorentzian profile on top of a linear background (Fig. 2B). At lower temperatures, two peaks are necessary: a broad peak (BP), very similar to that measured at higher temperature, and a narrow peak (NP) centered at a nearby value of H. We also scanned along K while fixing $H = H_{NP}$ at the maximum of the NP in the (H, 0) scan; there, the shape consists of a narrow and a broad peak, both centered at K = 0. Because the temperature dependence of the K-scans follows that of the H-scans (fig. S2) (28), the quasi-elastic peak in the reciprocal space can be modeled by a double 2D Lorentzian, a broad one and a narrow one, centered respectively at q_c^{NP} = (0.325, 0) and at q_c^{BP} = (0.295, 0) (Fig. 2E).

[1]Dipartimento di Fisica, Politecnico di Milano, I-20133 Milano, Italy. [2]Quantum Device Physics Laboratory, Department of Microtechnology and Nanoscience, Chalmers University of Technology, SE-41296 Göteborg, Sweden. [3]Dipartimento di Fisica, Università di Roma "La Sapienza," I-00185 Roma, Italy. [4]CNR-ISC, I-00185 Roma, Italy. [5]ESRF, European Synchrotron, F-38043 Grenoble, France. [6]Dipartimento di Fisica "E. Pancini," Università di Napoli Federico II, Complesso Monte Sant'Angelo, I-80126 Napoli, Italy. [7]CNR-SPIN, Complesso Monte Sant'Angelo, I-80126 Napoli, Italy. [8]CNR-SPIN, Dipartimento di Fisica, Politecnico di Milano, I-20133 Milano, Italy.
*Corresponding author. E-mail: riccardo.arpaia@chalmers.se (R.A.); giacomo.ghiringhelli@polimi.it (G.G.) †Present address: International Center for Quantum Materials, School of Physics, Peking University, CN-100871 Beijing, China.
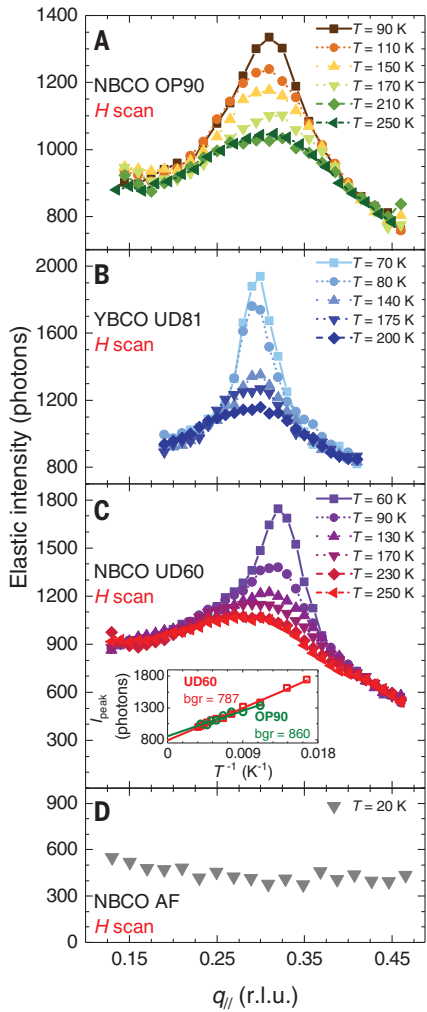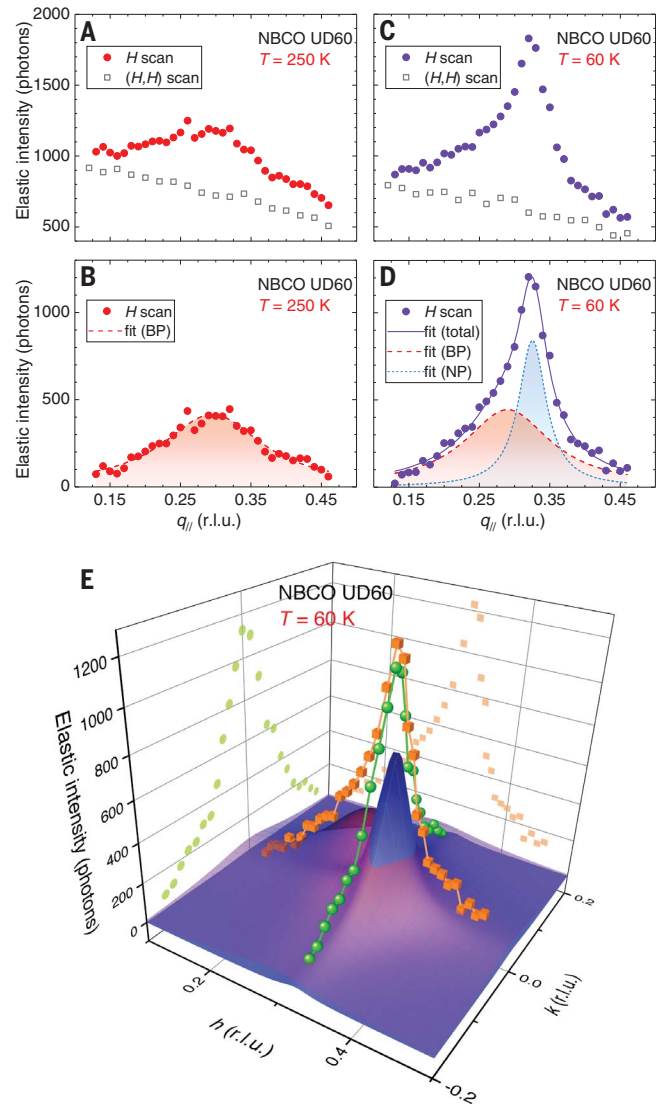
Fig. 1. Quasi-elastic scan along the (*H*, 0) direction for several YBa₂Cu₃O₇₋δ and Nd₁₊ₓBa₂₋ₓCu₃O₇₋δ films with different oxygen dopings. The quasi-elastic intensity was determined by integrating the Cu L_3 RIXS spectra measured at different $q_{||}$ values in the energy interval [−0.2 eV, +0.15 eV]. The measurements were performed at different temperatures on the following samples: (**A**) Optimally doped NBCO, $p \approx 0.17$. (**B**) Underdoped YBCO, $p \approx 0.14$. (**C**) Underdoped NBCO, $p \approx 0.11$. (**D**) Insulating NBCO, $p < 0.05$. The inset in (C) shows the peak intensity I_{peak} versus T^{-1} for samples OP90 (circles) and UD60 (squares). The extrapolation to $T \rightarrow \infty$ provides an estimate of the intrinsic background of the signal (bgr).

Fig. 2. Two distinct peaks in fits to NBCO UD60 data. (**A**) Quasi-elastic scan measured along (*H*, 0) on sample UD60 at $T = 250$ K (red circles). (**B**) After subtracting the linear background, given by the quasi-elastic scan measured along the Brillouin zone diagonal [open squares in (A)], a clear peak is still present, which can be fitted by a Lorentzian profile (dashed line). (**C**) Same as (A), but at $T = 60$ K (violet circles). (**D**) After subtracting the linear background [open squares in (C)], the data can be fitted with a sum of two Lorentzian profiles (solid line): one broader (dashed line), similar to that measured at 250 K, and the second one narrower and more intense (dotted line). (**E**) The 3D sketch shows the quasi-elastic scans measured along *H* (cubes) and along *K* (spheres) at $T = 60$ K on sample UD60, together with the Lorentzian profiles used to fit them. A narrow peak (NP, blue surface) emerges at $q_c^{NP} = (0.325, 0)$ from a much broader peak (BP, red surface) centered at $q_c^{BP} = (0.295, 0)$.

Figure 3 summarizes the outcome of the fittings for the samples UD60 and OP90, whereas fig. S6 reports the corresponding results for the UD81 sample. The NP presents all the characteristics previously observed in several underdoped cuprates and commonly attributed to the incommensurate CDWs. The BP shares with the NP the position in the reciprocal space (although with small differences; see fig. S7), but it

has a very different, almost constant, temperature dependence. Therefore, we attribute the BP to very short-range charge modulations (i.e., to CDFs), as depicted by the reddish region of the *T-p* phase diagram of Fig. 4A. Whereas the full width at half maximum (FWHM) of the NP follows a critical temperature dependence, the temperature dependence of the BP width is much weaker in the accessible temperature range and within our experimental uncertainties. Finally, although the amplitude of the NP (i.e., the peak height) is larger than that of the BP at low temperature, the total "volume" (i.e., the integrated scattering intensity) is always dominated by the BP, at least in the accessible *T* range above the critical temperature T_c (Fig. 3).

To further clarify the double character of the phenomenon and to assess the possible dynamical character of the CDFs, we studied the energy associated with the BP by exploiting the high resolution of our instruments. We measured Cu

L_3 RIXS spectra on the OP90 and UD60 samples at selected temperatures and at the wave vector of the BP maximum. At all temperatures, the main peak is slightly broader than the instrumental resolution (40 meV) and is not centered at zero energy loss, with the inelastic component stronger at higher *T* (fig. S10) (*28*). Contributions to this quasi-elastic peak come from phonons, from elastic diffuse scattering from the sample surface, and from charge fluctuations. The phonon peak intensity is either *T*-independent (for phonons with energies higher than 30 meV) or decreases upon cooling down (at lower energies); scattering from the surface is constant with *T*. The scattering related to CDWs is the only component expected to grow in intensity with decreasing *T*. Figure 4B shows the quasi-elastic component of three spectra taken on the optimally doped sample at 90 K, 150 K, and 250 K, and $q_{||} = (0.31, 0)$, after subtraction of the phonon contribution, as estimated from the (*H*, *H*) scan (see figs. S11 to S13 for details on how the
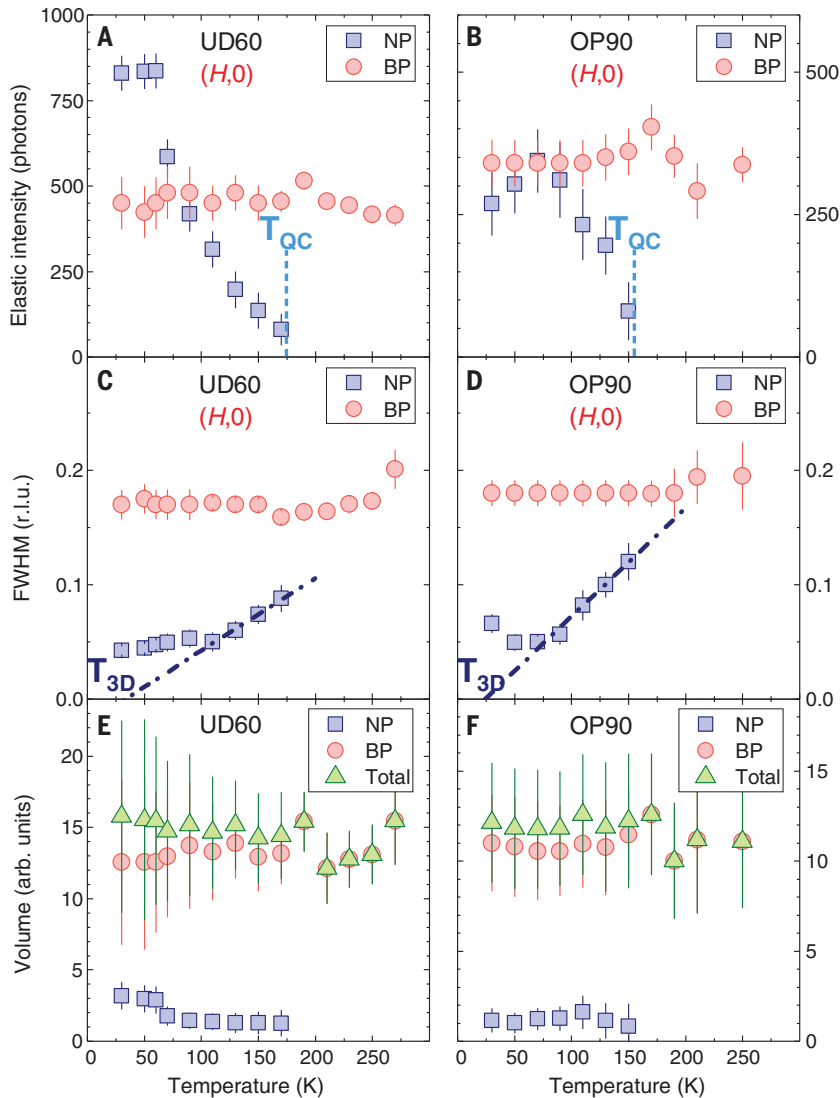
Fig. 3. Characteristics of the two charge density modulation peaks. The graphs show the temperature dependence of the parameters of the two Lorentzian profiles used to describe the quasi-elastic peaks of samples UD60 and OP90 (squares refer to the narrow peak, circles to the broad peak). (**A** and **B**) Intensity. (**C** and **D**) FWHM. T_{QC} is 175 K for sample UD60 and 155 K for sample OP90. T_{3D} is 33 K for sample UD60 and 24 K for sample OP90. (**E** and **F**) Volume of the charge density modulations. The total volume (triangles), given by the sum of the volumes of the two peaks, is dominated by the broad peak.

7 meV, indicating that the NP is associated with lower or null energy. Similar fittings for the UD60 sample give $\omega_0 \approx 6$ meV at high temperatures and 3 meV at 90 K (*28*).

The broad peak is therefore generated by dynamical CDFs, with pure 2D character related to individual CuO_2 planes, and is characterized by a noncritical behavior. Its ultrashort-range nature is confirmed by a correlation length—given by the FWHM $\propto \xi^{-1}$ values—of $2\xi \approx 4a$, which is comparable to the modulation period ($3.4a$; see fig. S8). The narrow peak, by contrast, comes from quasi-critical CDWs appearing only below the onset temperature T_{QC} (crosses in the phase diagram of Fig. 4A) (*28*). Quasi-critical CDW orders compete with superconductivity, as highlighted by the intensity and ξ saturation (or decrease) below T_c (Fig. 3 and figs. S4 to S6). In the relatively narrow temperature range above the occurrence of such competition, the linear extrapolation to zero of the NP width provides an estimate of the critical temperature T_{3D}, below which, in the absence of superconductivity, ξ would diverge (i.e., a static 3D CDW order would form). The values of T_{3D} of our three samples (Fig. 3, C and D, and fig. S6C), indicated as squares in the phase diagram of Fig. 4A, are in fairly good agreement with the onset of the long-range 3D CDWs (T_{3D}^H), obtained in high magnetic fields by NMR (*13*), and hard x-ray scattering experiments (*14*) (blue region in Fig. 4A). For OP90, T_{3D} is relatively low because the doping corresponds roughly to the p_c value of the QCP. Moreover, a scan taken at 62 K on overdoped YBCO (OD83, $p \approx 0.18$) shows that already at low temperatures, only the dynamical CDFs survive at $p > p_c$ (see fig. S9). Therefore, from the similarity between the T_{3D} in our films and the T_{3D}^H reported in the literature at the same oxygen doping levels, we can speculate that, were it not for the competing superconducting order that quenches the critical behavior of CDWs, 3D CDWs would occur for $p < p_c$ and $T < T_{3D}$ without any application of magnetic field. The static 3D CDW dome is centered at $p \approx 1/8$ and is delimited by two QCPs at $p \approx 0.08$ and 0.17 (*36, 37*); inside that doping range, above T_{3D} and below T_{QC}, quasi-critical CDWs—precursors of the static 3D CDWs—are present.

The phase diagram of Fig. 4A visualizes the scenario of a continuous crossover from the pure 2D dynamical CDF at high T and all dopings, to a quasi-critical CDW (still 2D) below T_{QC} and for $0.08 < p < 0.17$, to the static 3D CDW usually hindered by superconductivity. Although disregarded up to now, dynamical CDFs represent the bulk of the iceberg of the CDW phenomenon in cuprates. Indeed, they pervade a large part of the phase diagram and coexist with both quasi-critical CDWs and, possibly, 3D CDWs (Fig. 4A), and their total scattering intensity (the volume of the associated BP) dominates at all T (Fig. 3, E and F, and fig. S6E). Moreover, they do not compete with superconductivity.

This picture is consistent with the theoretical proposal of (*1, 25*). Owing to the weak coupling of CuO_2 planes, CDW orders have a marked 2D
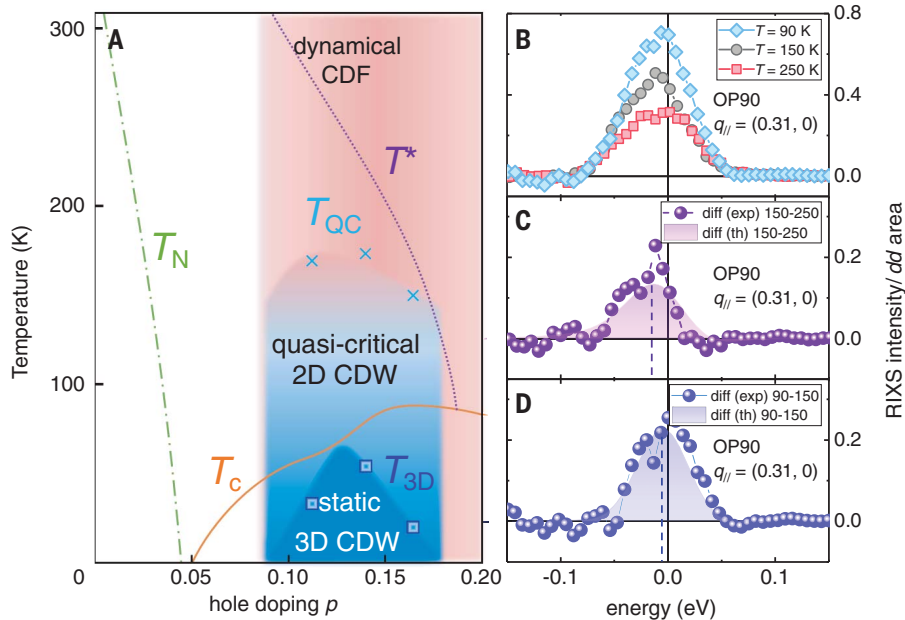
additional phonon contribution and elastic scattering were subtracted). To better extract the charge density contribution, we subtracted the higher-T spectra from the lower-T ones; in Fig. 4, C and D, we show the 150 K–250 K and 90 K–150 K difference spectra. The resulting peaks are narrower than the original spectra. The higher-T difference is evidently centered at $\omega_0 \approx 15$ meV, whereas the lower-T difference is almost elastic. This means that the BP, still dominant at high T, has a fluctuating nature, whereas the NP emerges at lower T as a nearly static, quasi-critical CDW.

These results can be interpreted within the theory mentioned above, based on the charge density instability of the high-doping correlated Fermi liquid (*1, 23, 24*). We fitted the three quasi-elastic peaks in Fig. 4B (see also fig. S11) by using the dynamical charge susceptibility, proportional to the correlation function of the density fluctuations $\langle n(q, \omega)n(-q, \omega)\rangle$ in Fourier space, as obtained from a standard dynamical Ginzburg-Landau approach in Gaussian approximation (*34, 35*). Its imaginary part, multiplied by the Bose function, gives the response function for the charge density modulation and represents the intensity of the low-energy peak in the RIXS spectra $I(q, \omega)$. Then the spectra in Fig. 4B can be fitted with this theory, assuming a characteristic energy $\omega_0 \approx 15$ meV for these overdamped charge fluctuations at 150 K and 250 K; the 90 K curve is better fitted with $\omega_0 \approx$

Fig. 4. Static and dynamic charge order in the phase diagram of the HTS cuprates. (A) The *T-p* phase diagram of cuprates is typically marked by the antiferromagnetic, pseudogap, and superconducting regions (respectively characterized by the onset temperatures T_N, T^*, and T_c). Our results prove that most of these regions are pervaded by charge density modulations of some sort. The narrow peak describes the CDWs, manifesting in a region (pale blue) below T_{QC} (crosses). These 2D CDWs are quasi-critical and are precursors of the static 3D CDWs (blue region). Even though we cannot directly access this dome without a magnetic field, the temperatures T_{3D} (squares) that we infer from the *T* dependence of the NP FWHM are in agreement with those previously determined by NMR and hard x-ray scattering experiments (*15*, *16*). The broad peak describes short-range charge density fluctuations (CDFs), which dominate the phase diagram (red region), coexisting both with the quasi-critical 2D CDWs and with superconductivity, and persisting even above T^*. In contrast, CDFs disappear in undoped/antiferromagnetic samples (white region), whereas their occurrence between $p \sim 0.05$ and $p \sim 0.08$ has yet to be determined. To evaluate the characteristic energies ω_O associated with the BP, we measured high-resolution RIXS spectra at various temperatures on the samples OP90 and UD60. **(B)** Quasi-elastic component of the spectra (after subtraction of the phonon contribution) at T = 90, 150, and 250 K, measured on sample OP90 at $q_{||}$ = (0.31, 0). **(C and D)** The experimental 150 K–250 K and 90 K–150 K difference spectra, presented in (B), are shown (spheres), together with the theoretical calculation (solid areas). The data are in agreement with the theory, assuming $\omega_O \approx 15$ meV at 150 and 250 K and $\omega_O \approx 7$ meV at 90 K [dashed lines in (C) and (D)].

character and, because of strong quantum thermal dynamical fluctuations, they acquire a truly static character only below T_{3D}. For YBCO and NBCO, T_{3D} is smaller than T_c, thus requiring strong magnetic fields or epitaxially grown samples to suppress superconductivity to obtain static 3D CDWs.

Although this theory can explain most of the experimental findings, some questions remain open. Other cuprate families will have to be tested and the doping region extended to confirm the general applicability of the dynamic CDF scenario. A BP, centered at $q_{||} \approx q_c^{NP}$ and persisting at high temperatures, has been observed over the past few years in other cuprates (*13*, *38*), pointing toward a universality of the CDF phenomenon. However, none of the aforementioned experiments has been conclusive in this respect, because a complete temperature dependence and/or a discrimination of the quasi-elastic

signal from the inelastic one was missing. The actual relation between the quasi-critical CDW and the dynamical CDF must also be fully clarified, with particular reference to the possible spatial separation or coexistence of the two phenomena, ultimately linked to the role of disorder in the samples studied by scanning tunneling microscope (*7*, *39*, *40*) and micro–x-ray scattering (*41*) experiments.

The most intriguing finding of this work is the ubiquitous presence (both in temperature and doping) of a broad peak caused by dynamical CDFs, which have small energies of a few meV and extend over a broad momentum range. Therefore, they provide quite an effective low-energy scattering mechanism for all the quasi-particles on the Fermi surface. This makes these excitations an appealing candidate for producing the linear temperature dependence of the resistivity in the normal state and other marginal Fermi

liquid phenomena that, since the early days of HTS (*42*), have been the most prominently peculiar properties of the cuprates.

REFERENCES AND NOTES

1. C. Castellani, C. Di Castro, M. Grilli, *Phys. Rev. Lett.* **75**, 4650–4653 (1995).
2. C. Castellani, C. Di Castro, M. Grilli, *Z. Phys. B* **103**, 137–144 (1996).
3. S. A. Kivelson et al., *Rev. Mod. Phys.* **75**, 1201–1241 (2003).
4. V. J. Emery, S. A. Kivelson, *Physica C* **209**, 597–621 (1993).
5. J. M. Tranquada, B. J. Sternlieb, J. D. Axe, Y. Nakamura, S. Uchida, *Nature* **375**, 561–563 (1995).
6. A. Bianconi et al., *Phys. Rev. Lett.* **76**, 3412–3415 (1996).
7. C. Howald, H. Eisaki, N. Kaneko, M. Greven, A. Kapitulnik, *Phys. Rev. B* **67**, 014533 (2003).
8. M. Vershinin et al., *Science* **303**, 1995–1998 (2004).
9. J. E. Hoffman et al., *Science* **295**, 466–469 (2002).
10. T. Wu et al., *Nat. Commun.* **6**, 6438 (2015).
11. G. Ghiringhelli et al., *Science* **337**, 821–825 (2012).
12. J. Chang et al., *Nat. Phys.* **8**, 871–876 (2012).
13. R. Comin, A. Damascelli, *Annu. Rev. Condens. Matter Phys.* **7**, 369–405 (2016).
14. E. H. da Silva Neto et al., *Phys. Rev. B* **98**, 161114 (2018).
15. T. Wu et al., *Nature* **477**, 191–194 (2011).
16. S. Gerber et al., *Science* **350**, 949–952 (2015).
17. M. Blüschke et al., *Nat. Commun.* **9**, 2978 (2018).
18. Y. Y. Peng et al., *Nat. Mater.* **17**, 697–702 (2018).
19. P. W. Anderson, *Science* **235**, 1196–1198 (1987).
20. P. W. Anderson, *Phys. Rev. Lett.* **64**, 1839–1841 (1990).
21. X.-G. Wen, P. A. Lee, *Phys. Rev. Lett.* **76**, 503–506 (1996).
22. T. M. Rice, K.-Y. Yang, F. C. Zhang, *Rep. Prog. Phys.* **75**, 016502 (2012).
23. R.-G. Cai, L. Li, Y.-Q. Wang, J. Zaanen, *Phys. Rev. Lett.* **119**, 181601 (2017).
24. S. Sachdev, E. Berg, S. Chatterjee, Y. Schattner, *Phys. Rev. B* **94**, 115147 (2016).
25. S. Andergassen, S. Caprara, C. Di Castro, M. Grilli, *Phys. Rev. Lett.* **87**, 056401 (2001).
26. S. Caprara, C. Di Castro, G. Seibold, M. Grilli, *Phys. Rev. B* **95**, 224511 (2017).
27. X. Montiel, T. Kloss, C. Pépin, *Phys. Rev. B* **95**, 104510 (2017).
28. See supplementary materials.
29. M. Salluzzo et al., *Phys. Rev. B* **72**, 134521 (2005).
30. R. Arpaia, E. Andersson, E. Trabaldo, T. Bauch, F. Lombardi, *Phys. Rev. Mater.* **2**, 024804 (2018).
31. R. Comin et al., *Science* **343**, 390–392 (2014).
32. T. P. Croft, C. Lester, M. S. Senn, A. Bombardi, S. M. Hayden, *Phys. Rev. B* **89**, 224513 (2014).
33. The reason is the large background of the energy-integrated resonant x-ray scattering scans, caused by the various inelastic contributions resolved in the RIXS spectra (often improperly called "fluorescence" background). In the attempt to single out the CDW contribution, a reference scan measured at "high" temperature and meant to be the intrinsic background was subtracted out from the low-*T* scans, therefore assigning the charge order contribution exclusively to the *T*-dependent part of the signal.
34. J. A. Hertz, *Phys. Rev. B* **14**, 1165–1184 (1976).
35. A. J. Millis, *Phys. Rev. B* **48**, 7183–7196 (1993).
36. S. Badoux et al., *Nature* **531**, 210–214 (2016).
37. H. Jang et al., *Phys. Rev. B* **97**, 224513 (2018).
38. H. Miao et al., *Proc. Natl. Acad. Sci. U.S.A.* **114**, 12430–12435 (2017).
39. S. H. Pan et al., *Nature* **413**, 282–285 (2001).
40. Y. Kohsaka et al., *Phys. Rev. Lett.* **93**, 097004 (2004).
41. G. Campi et al., *Nature* **525**, 359–362 (2015).
42. C. M. Varma, P. B. Littlewood, S. Schmitt-Rink, E. Abrahams, A. E. Ruckenstein, *Phys. Rev. Lett.* **63**, 1996–1999 (1989).
43. R. Arpaia et al., Raw data for "Dynamical charge density fluctuations pervading the phase diagram of a Cu-based high-T_c superconductor"; http://dx.doi.org/10.5281/zenodo.2641214 (2019).

SUPPLEMENTARY MATERIALS

science.sciencemag.org/content/365/6456/906/suppl/DC1
Materials and Methods
Supplementary Text
Figs. S1 to S13
References (*44–54*)

16 August 2018; accepted 30 July 2019
10.1126/science.aav1315